

FBOTs and AT2018cow following electron-capture collapse of merged white dwarfs

Maxim Lyutikov

Department of Physics, Purdue University, 525 Northwestern Avenue, West Lafayette, IN 47907-2036

and

Silvia Toonen

Astronomical Institute Anton Pannekoek, University of Amsterdam, P.O. Box 94249, 1090 GE, Amsterdam

ABSTRACT

We suggest that fast-rising blue optical transients (FBOTs), and the brightest event of the class AT2018cow, result from electron-capture collapse following a merger of a massive ONeMg white dwarf (WD) with another WD. Two distinct evolutionary channels lead to the disruption of the less massive WD during the merger and formation of a shell burning non-degenerate star incorporating the ONeMg core. During the shell burning stage a large fraction of the envelope is lost to the wind, while mass and angular momentum are added to the core. As a result, the electron-capture collapse occurs with a small envelope mass, after $\sim 10^2 - 10^4$ years. During the formation of a neutron star as little as $\sim 10^{-2}M_{\odot}$ of the material is ejected at the bounce-off with mildly relativistic velocities and total energy \sim few 10^{50} ergs. This ejecta becomes optically thin on time scales of days - this is the FBOT. During the collapse the neutron star is spun up and magnetic field is amplified. The ensuing fast magnetically-dominated relativistic wind from the newly formed neutron star shocks against the ejecta, and later against the wind. The radiation-dominated forward shock produces the long-lasting optical afterglow, while the termination shock of the relativistic wind produces the high energy emission in a Pulsar Wind Nebulae-like manner. The late X-ray variability is akin to magnetically-driven Crab flares (and possibly late GRB flares). If the secondary WD was of the DA type - the most frequent - the wind will have hydrogen, of the order of $10^{-4}M_{\odot}$: this explains appearance of hydrogen late in the afterglow spectrum. The model explains many of the puzzling properties of FBOTs/AT2018cow: host galaxies, fast and light anisotropic ejecta producing bright optical peak, afterglow high energy emission of similar luminosity to optical, hard X-ray and infra-red features, presence of dense wind environment, late powerful radio emission.

1. Introduction

AT2018cow (Smartt et al. 2018; Perley et al. 2018; Ho et al. 2018; Margutti et al. 2018) is a mysterious astrophysical event. It is likely to be the brightest member of the class of fast-rising blue optical transient (FBOT, Drout et al. 2014). AT2018cow seems to be at a cross-road of supernova explosion (and associated complicated nuclear reactions, neutrino transports physics), pulsars/magnetars, (early) pulsar wind nebulae (PWNe), possibly, GRBs and, possibly, white dwarf physics.

AT2018cow had a few surprising features, most important in our view being:

- optical rise-time of ≤ 3 days - this is order of magnitude shorter than the supernovae
- peak optical luminosity $\sim 4 \times 10^{44}$ erg s^{-1} - this exceeds the typical peak power of supernovae
- The X-ray emission of initial power $\sim 10^{43}$ erg s^{-1} had an extra component at $t \leq 15$ days, peaking at ~ 40 keV (Fig. 6 in Margutti et al. 2018)

- There is a clear change of properties of the emission at ~ 20 days.
- There is an indication of the rising IR component at $t \geq 30$ days (Fig. 5 in [Perley et al. 2018](#))
- There is bright radio emission $t \geq 80$ day peaking at $\sim 10^{10}$ Hz (Fig. 11 in [Margutti et al. 2018](#))

These properties exclude normal Ni-powered supernovae and require a separate formation channel. We discuss one such possible channel in the present paper, trying to build a coherent model of AT2018cow.

2. The model: a specific channel of WD mergers

In this paper we discuss a scenario where fast-rising blue optical transients (FBOTs) are powered by the electron-capture collapse following a merger of a massive ONeMg white dwarf (WD) with another WD. (Previously, the electron-capture collapse was mostly used in the accretion models, *e.g.*, [Canal & Schatzman 1976](#), hence the name Accretion Induced Collapse, AIC.); see also [Timmer & Woosley \(1992\)](#); [Miyaji et al. \(1980\)](#); [Nomoto & Kondo \(1991\)](#); [Kitaura et al. \(2006\)](#); [Jones et al. \(2016\)](#) Some details of the binary evolution and of the collapse in such systems were previously discussed by [Lyutikov & Toonen \(2017\)](#), see also [Brooks et al. \(2017\)](#); [Ruiter et al. \(2018\)](#); [Yungelson & Kuranov \(2017\)](#).

Let us outline the main stages (see [Lyutikov & Toonen 2017](#), for a more detailed discussion); also [Ruiter et al. \(2018\)](#). An initial system with the primary mass $M_1 \sim 6 - 10 M_\odot$ and the secondary mass $M_2 \sim 3 - 6 M_\odot$ forms a double degenerate CO-ONeMg WD system, via two distinct evolutionary channels ([Lyutikov & Toonen 2017](#)). For sufficiently large mass ratio $q \equiv M_2/M_1 > q_{crit} \sim 0.25$ ([Marsh et al. 2004](#)) the ensuing gravitational wave-driven mass transfer is unstable, whereby the less massive CO WD is disrupted on a few orbital time scales and forms a disk around the primary. Disk accretion at high rates creates a spreading layer - a belt-like structure on the surface of the primary ([Inogamov & Sunyaev \(1999\)](#); [Balsara et al. \(2009\)](#); [Inogamov & Sunyaev \(2010\)](#); [Belyaev et al. \(2013\)](#); [Philippov et al. \(2016\)](#)). After the spreading is complete (on viscose time scale of $\sim 10^4$ seconds, *e.g.*, [Shen et al. 2012](#)) the resulting star of $\sim 2M_\odot$ consists of a slowly rotating degenerate ONeMg core, and a fast rotating, with period in the hundreds of seconds, non-degenerate envelope. After the removal of the degeneracy the envelope expands to $R_* \sim \text{few } 10^9$ cm. The star will emit near the Eddington limit and drive powerful winds. Angular momentum contained in the shell will be both lost to the wind, and transported to the core through the (turbulent) boundary layer.

The merger product ignites shell CO burning, adding mass to the degenerate core; at the same time mass and angular momentum is lost due to powerful winds. For an ONeMg WD sufficiently close to the Chandrasekhar mass an electron-capture/accretion induced collapse follows after $\sim 10^2 - 10^4$ years later. During the collapse the magnetic field is amplified, [Mösta et al. \(2015\)](#) and the neutron star is spun to millisecond periods. As a result it produces long lasting relativistic wind that shocks against the ejecta material and, later on, against material lost during the shell-burning stage. The highly magnetized relativistic wind produced by a central neutron star will interact with the fairly dense newly ejected material and dense pre-AIC wind, producing *X*-ray afterglow in the *highly magnetized reverse shock*, in a way similar to the case of afterglows from long GRBs, as suggested by [Lyutikov & Camilo Jaramillo \(2017\)](#).

In Fig. 1 we picture the immediate surrounding of a FBOT at times \sim days-weeks after the collapse. This picture is our working model.

The key point of the model is that a merger of a heavy ONeMg WD with another WD, and ensuring mass loss during the shell burning stage, results in a collapse of the core surrounded by a fairly light envelope, tens of percent of M_\odot at most. Depending on the particular collapse time one expects few cases when the AIC happens right before the shell burning is about to end. This would produce fast ejecta with small mass and leads to AT2018cow-like events. In

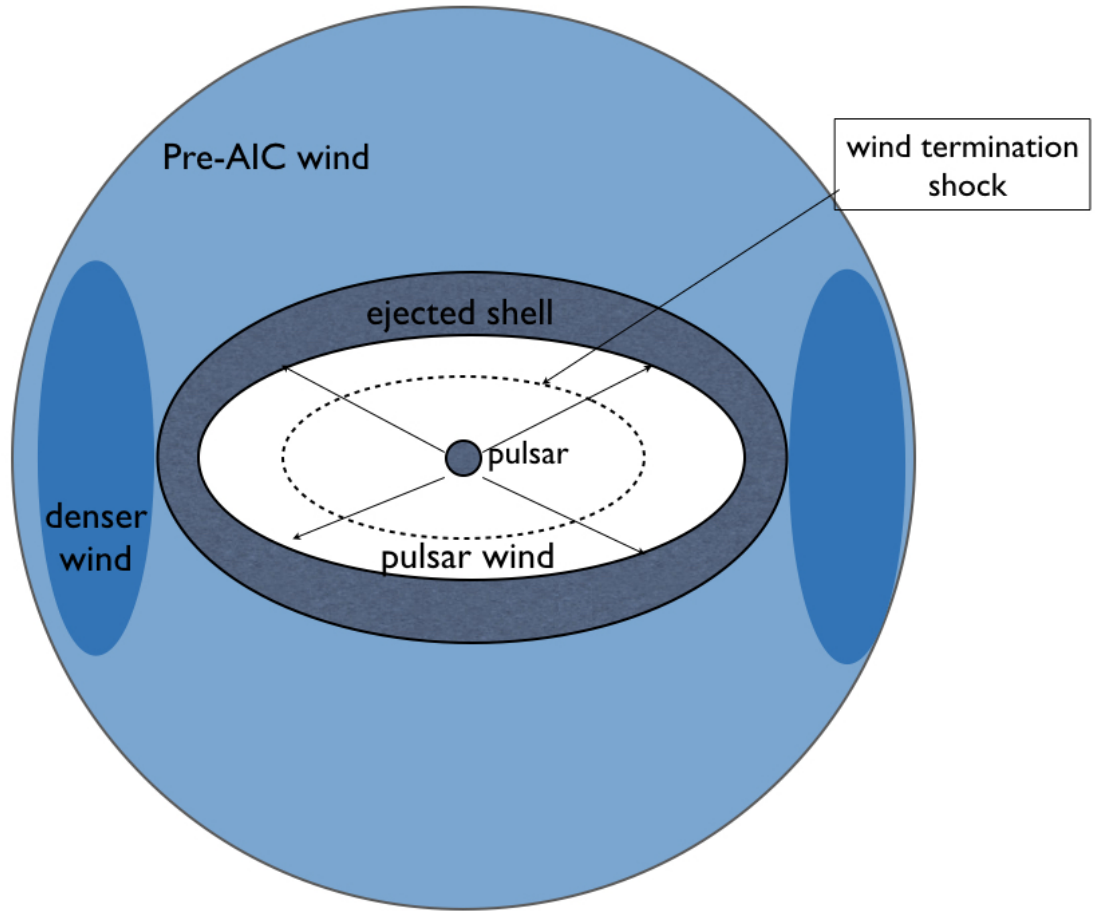


Fig. 1.— Immediate surrounding of a FBOTs: the remaining NS generates pulsar-like wind (highly relativistic, highly magnetized), that interacts with the bounced-ejected shell, and the wind from the shell burning stage. Both pulsar winds and the ejected shell are equatorially collimated.

other cases, envelopes of few tenths of solar masses are ejected, producing longer and less bright transients, which are still fast and luminous if compared with conventional supernovae.

In addition, to spinning up the core large amount of angular momentum of the shell (disrupted secondary WD) is lost to the wind. As a result the AIC can be direct, without formation of the accretion disk. In this case the newly born neutron star loses most of its rotational energy to the fast, relativistic wind. For shorter shell-burning stage, there is too much angular momentum in the shell, that leads to the formation of the accretion disk, that spins down the central neutron star in a propeller stage. As a result, a large fraction of the energy is deposited into relatively slow, matter-dominated wind with low radiation efficiency.

Regarding the origin of Type Ia SNe, our model is both somewhat independent of the active discussions on single versus double degenerate/mixed origin of SNIa (in a sense that it can work in both cases), but at the same time the

model is closely related to the controversy. In any case, the merger of ONeMg-CO WDs will likely proceed in a regime different to the more common CO WDs merger.

3. The pre-collapse wind and the ejecta

3.1. Pre-collapse wind

Let's assume that the post-merger/shell-burning star launches a wind with velocity V_w . After time t_w the edge of wind reaches radius $r_{max} = R_* + V_w t_w$. For a total mass in the wind M_{env} we find

$$\begin{aligned}\rho_w &= \frac{\dot{M}}{4\pi r^2 V_w} \\ M_{env} &= \int_{R_*}^{R_* + V_w t_w} \rho_w 4\pi r^2 dr = \dot{M} t_w \\ t_w &= \frac{M_{env}}{\dot{M}}\end{aligned}\tag{1}$$

For mass loss rate of $\dot{M} = 10^{-3} M_\odot \text{ yr}^{-1}$ and total mass in the envelope of $\sim 0.5 M_\odot$ this stage lasts $t_w \sim 5 \times 10^2$ yrs; we adopt notation $x_n = X/10^n$.

Optical depth through the wind is ~ 1 at

$$r_w = \frac{\sigma_R \dot{M}}{4\pi m_p V_w} = 2 \times 10^{13} \dot{m}_{-3} V_{w,8}^{-1} \text{cm}\tag{2}$$

3.2. Ejecta

As the shell is accreted onto the proto-neutron star, a narrow outer layer will be ejected. Previously, studies of the AIC ejected mass are predict $\sim 10^{-3} - 10^{-1} M_\odot$ ejected (Woosley & Baron 1992; Fryer et al. 1999; Abdikamalov et al. 2010).

These studies were mostly concerned with single degenerate scenario of AIC, basically with no envelope. It is not clear how a presence of a tenuous envelope, of few $0.1 M_\odot$, would affect the ejecta mass. Let us assume, for a particular case of AT2018cow, a bounced ejected mass of M_{ej} , with maximal velocity $V_{ej,0}$. For homologous expansion with $v \propto r$, the energy in the ejected part is

$$E_{ej} = \frac{3}{10} M_{ej} V_{ej,0}^2\tag{3}$$

Before the ejecta slows down due to the interaction with the pre-existing wind, its density evolves according to

$$\rho_{ej} = \frac{3}{4\pi} \frac{M_{ej}}{(V_{ej,0} t_{ej})^3}\tag{4}$$

where $V_{ej,0}$ is the maximum velocity of the ejecta.

For numerical estimates we chose $M_{ej} \approx 10^{-2} m_{ej,-2} M_\odot$. (Many of the final relations depend weakly on ejecta mass, $\propto M_{ej}^{1/4}$, e.g., Eq. (16) and (18)). The velocity of the ejecta will be related to the escape velocity from the proto-neutron star,

$$V_{ej,0} \approx \sqrt{\frac{GM_{NS}}{R_{proto-NS}}} = 7 \times 10^9 \text{cms}^{-1} = 0.26c\tag{5}$$

for a proto-neutron star radius of $R_{proto-NS} = 30\text{km}$. The ejecta energy is then $E_{ej} \approx 4 \times 10^{50} m_{ej,-2}$ erg. Thus, our model naturally produces fast and light ejecta.

The Thomson optical depth through ejecta is

$$\tau_{ej} = \frac{\rho_{ej}}{m_p} \sigma_T V_{ej,0} t = \frac{3}{4\pi} \frac{M_{ej} \sigma_T}{m_p (V_{ej,0} t)^2} = 3 m_{ej,-2} t_d^{-2} \quad (6)$$

where t_d is time in days since the explosion. The surface $\tau = 1$ evolves with time according to

$$r_{ej,\tau=1} = V_0 t \left(1 - \frac{2\pi}{5} \frac{m_p V_0^4}{E_{ej} \sigma_T} \right) \quad (7)$$

It reaches maximum at

$$\begin{aligned} t_{ej,max} &= \sqrt{\frac{5}{6\pi}} \sqrt{E_{ej} \sigma_T m_p V_0^4} \approx 1 m_{ej,-2}^{1/2} \text{day} \\ r_{ej,max} &= \sqrt{\frac{10}{27\pi}} \sqrt{E_{ej} \sigma_T m_p V_0^2} \approx 5 \times 10^{14} m_{ej,-2}^{1/2} \text{cm} \end{aligned} \quad (8)$$

This explains the short rise time of the transient. Also note that radius (8) is larger than the radius (2) when the wind becomes optically thin. Thus, the maximum of the ejecta emission is not affected by scattering in the pre-explosion wind.

In fact, for the expanding optically thick plasma the peak in luminosity will appear before the shell becomes optically thin due to the fact that photons diffuse out somewhat faster (Arnett 1982). The peak time is

$$t_{pk} \approx \sqrt{\frac{M_{ej} \kappa}{4\pi V_{ej,0} c}} \approx 0.4 m_{ej,-2} \text{days} \quad (9)$$

where $\kappa \approx 0.1 \text{ cm}^2 \text{ g}^{-1}$ is an estimate of the effective opacity due to electron scattering. Estimates (6) and (9) explain the short rise time of the optical light curve.

The free-free emission of the optically thin part of the ejecta is fairly small,

$$\begin{aligned} L_{ej,ff} &\approx j_{ff} n_{ej}^2 (V_{ej,0} t)^3 = 4 \times 10^{39} \text{erg s}^{-1} m_{ej,-2}^2 T_4^{1/2} t_d^{-3} \\ j_{ff} &= 2.4 \times 10^{-27} \sqrt{T} n^2 \end{aligned} \quad (10)$$

where j_{ff} is free-free emissivity (Lang 1999). Thus, we associated the early fast optical transient with the emission of the ejected shell.

3.3. Ejecta-wind interaction

The ejecta will launch a forward shock into the pre-explosion wind. As the shock propagates through the wind the accumulated mass is then

$$M_{acc} \approx \dot{M} t \frac{V_{ej,0}}{V_w} \quad (11)$$

It becomes equal the ejecta mass at

$$t_{slow} = \frac{M_{ej}}{\dot{M}} \frac{V_w}{V_{ej,0}} \rightarrow 4 \times 10^6 m_{ej,-2} V_{w,8} \dot{m}_{-3}^{-1} \text{sec} \quad (12)$$

Thus, the external wind has little effect on the ejecta until a approximately a month after the explosion. Before that the ejecta is in free expansion stage.

This will be approximately the time that the NS-driven shock exits the ejecta and enters the wind. We associate this with the transition of the afterglow properties at ~ 20 days (Margutti et al. 2018).

4. Non-thermal emission in FBOTs: pulsar-like termination shock in fast NS wind

4.1. Wind power

The newly created neutron star (NS) is spun up to short periods and magnetic field is amplified. The central NS will produce a highly magnetized wind that shocks against the ejecta (and, later on, against the pre-explosion wind). The NS wind-ejecta interaction will produce two shocks: forwards shock in the ejecta and termination shock in the wind. It is the wind termination shock that produces the X-ray emission, while the radiation-dominated forward shock produces the optical transient, see §4.4. In the termination shock the accelerated particles will produce synchrotron emission in the fast cooling regime, so that a large fraction of the wind power will be emitted as radiation. (See Lyutikov & Camilo Jaramillo 2017, for discussion of emission produced at the highly magnetized termination shock in GRBs).

In the fast cooling regime most of the power given to the accelerated particles is emitted. Let us then identify the observed X-ray luminosity with NS wind power. It is nearly constant at $L_0 \approx 10^{43}$ erg s $^{-1}$ until $t_\Omega \sim 20$ days and then falls $\propto t^{-2}$ (Fig. 5 in Margutti et al. 2018). Using the initial pulsar spin-down power and spin-down time t_Ω , we find the magnetic field and the initial spin

$$\begin{aligned} B_{NS} &\approx \frac{c^{3/2} I_{NS}}{\sqrt{L_0} R_{NS}^3 t_\Omega} = 8 \times 10^{14} \text{ G} \\ \Omega_0 &= \sqrt{\frac{L_0 t_\Omega}{I_{NS}}} = 140 \text{ rads}^{-1} \end{aligned} \quad (13)$$

At $t > t_\Omega$ we have $L \propto t^{-2}$. Thus we suggest that a magnetar-type object is formed; its initial spin is not very high - 45 milliseconds. The wind power at time t is then

$$L_w = \frac{L_{w,0}}{(1 + t/t_\Omega)^2} \quad (14)$$

(In fact, since observed X-ray luminosity is a lower limit on wind power, estimates (13) are upper limit on magnetic field and lower limit on the initial spin.

4.2. Propagation of NS wind-driven shock through ejecta

The newly formed neutron star generates powerful wind that first propagates within the ejecta, and later on through the pre-explosion wind. Let us consider the dynamic of the wind-driven shock propagating through ejecta with density (4). In the Kompaneets approximation (Kompaneets 1960)¹, the relativistic wind with power L_w will produce a cavity expanding according to

$$\frac{L_w}{4\pi R^2 c} = \rho_{ej} \left(\partial_t R - \frac{R}{t} \right)^2 \quad (15)$$

¹Kompaneets approximation assumes supersonic driving, while Sedov scaling assumes subsonic driving of the expansion. At early times, when the termination shock is close to the contact discontinuity, the Kompaneets approximation is more justified than the Sedov's.

Given the wind power (14) and density (4) this gives

$$R_{PWN} \approx \frac{(L_{w,0}t_\Omega)^{1/4}V_{ej,0}^{3/4}}{(cM_{ej})^{1/4}}t\sqrt{\arctan \sqrt{t/t_\Omega}} = \begin{cases} \frac{L_{w,0}^{1/4}V_{ej,0}^{3/4}}{(cM_{ej})^{1/4}}t^{5/4}, & t \rightarrow 0 \\ \sqrt{\frac{\pi}{2}}\frac{(L_{w,0}t_\Omega)^{1/4}V_{ej,0}^{3/4}}{(cM_{ej})^{1/4}}t, & t \rightarrow \infty \end{cases} \quad (16)$$

(function $x\sqrt{\arctan \sqrt{x}}$ has limits $x^{5/4}$ for $x \ll 1$ and $\sqrt{\pi/2}x$ for $x \gg 1$). For example, at one day the neutron star produces a cavity if a size $R \approx 6 \times 10^{13}m_{ej,-2}^{-1/4}$.

The relative velocity of the shock with respect to the ejecta is

$$V_s = 0.37\frac{(L_{w,0}t)^{1/4}V_{ej,0}^{3/4}}{(cM_{ej})^{1/4}} = 2 \times 10^8 t_d^{1/4} m_{ej,-2}^{1/4} \text{ cm s}^{-1} \quad (17)$$

Thus, it changes only slowly with time.

The corresponding equipartition post-termination shock magnetic field (in the highly magnetized wind) is

$$B = \frac{\sqrt{2L_w}}{\sqrt{cR}} = \sqrt{2}\frac{L_{w,0}^{1/4}M_{ej}^{1/4}}{c^{1/4}V_{ej,0}^{3/4}}\left(t^{5/4}\sqrt{1+t/t_\Omega}\right)^{-1} \approx 300\text{G}m_{ej,-2}^{1/4}\left(t_d^{5/4}\sqrt{1+0.05t_d}\right)^{-1} \quad (18)$$

(t_d is time measured in days.) Thus, at early times magnetic field $B \propto t^{-5/4}$, while later $B \propto t^{-7/4}$.

Also note that the NS-driven shock never overtakes the freely expanding ejecta (radius (16) is always smaller than $V_{ej,0}t$). The shock breaks out hydrodynamically from the ejecta into the preexisting wind when ejecta starts to decelerate at (12), after approximately a month.

4.3. Propagation of NS wind-driven shock through pre-explosion ejecta

The Kompaneets approximation (15), in the pre-explosion wind profile (1), with wind power given by (14) gives

$$R_{PWN} = \sqrt{\frac{L_{w,0}v_w}{c\dot{M}}}t \ln \frac{t}{t+t_\Omega} \quad (19)$$

Neglecting the slow-varying logarithm (the Kompaneets approximation is expected to be less applicable at later times)

$$V_s \approx \sqrt{\frac{L_{w,0}v_w}{c\dot{M}}} = 7 \times 10^8 V_{w,8}^{1/2} \dot{m}_{-3}^{-1/2} \text{ cm s}^{-1} \quad (20)$$

Thus, after break-out the expansion accelerates mildly, *cf.* Eq. (17).

The equipartition magnetic field is then

$$B = \frac{\sqrt{2L_w}}{\sqrt{cR}} = \sqrt{\frac{2\dot{M}}{v_w}}\frac{1}{t} = 350\dot{m}_{-3}^{1/2}V_{w,8}^{-1/2}t_d^{-1} \text{ G}. \quad (21)$$

It is similar (both in value and in time-dependence) to the magnetic field before the NS wind breaks out of the ejecta.

4.4. Optical emission: forward shock from the NS-driven wind

The NS wind is shocked at the termination shock and will also produce a forward shock. Similar amount of energy will be dissipated in both shocks. Particles accelerated at the termination shock produces the non-thermal X-ray emission, while the forward shock will produce the long lasting optical emission (in addition to the emission produced by the ejecta).

Let us first consider the forward shock emission. The forward shock initially propagates through the ejecta, and later-on through the pre-explosion wind. The shock driven by the NS wind will be modified by radiation pressure, (Weaver 1976; Budnik et al. 2010; Ofek et al. 2010; Lyutikov 2018). The observed properties of mildly relativistic shocks are fairly complicated and often have steep dependence on the underlying parameters due to steep dependence of photon production rates, photon escape and pair production on the plasma properties. Qualitatively, radiation-dominated shocks can temporarily reach temperature exceeding the shock jump conditions (even taking into account radiation pressure). For fast photon production this may result in isothermal jumps (Landau & Lifshitz 1959; Lyutikov 2018), in which case the peak temperature exceeds the final temperature by a factor of a few. For slow photon production the temperature peak may exceed the final temperature by a large amount (Ito et al. 2018; Ioka et al. 2018).

Let us give here an order-of-magnitude estimate of the *final* post-shock temperature in strongly radiationally-dominated shock. The post shock pressure is

$$p_{FS} \sim \frac{L_w}{4\pi R_{PN}^2 c} = \frac{\sqrt{3}}{16\pi} \frac{\sqrt{L_{w,0} M_{ej}}}{\sqrt{c} V_{ej,0}^{3/2} t^{5/2}} \quad (22)$$

The post-shock pressure is contributed both by matter pressure, $\sim nT$ and radiation pressure $\sim 4\sigma_{SB}T^4/c$. Radiation pressure dominates for (Weaver 1976; Budnik et al. 2010; Ofek et al. 2010; Lyutikov 2018)

$$V_s \gg \frac{(\rho \lambda_C^3)^{1/6} c}{m_e \mu^{2/3}} \approx 10^5 m_{ej,-2}^{1/6} t_d^{-1/2} \text{ cm s}^{-1} \quad (23)$$

where $\lambda_C = \hbar/(m_e c)$ and $\mu = m_p/m_e$. Comparing with (17) we conclude that the forward shock is radiation-dominated with post-shock temperature (far downstream!)

$$T_{FS} \approx \left(\frac{c L_{w,0} M_{ej}}{\sigma_{SB}^2 V_{ej,0}^3 t^5} \right)^{1/8} = 4 \times 10^4 m_{ej,-2} t_d^{-5/8} \text{ K} \quad (24)$$

This matches the observed temperatures at early times, both in value and (presumably) the temporal decrease (Margutti et al. 2018).

On the other hand, radiation-dominated shocks require sufficiently high optical depth, at least of the order of $\tau \sim c/V_s$, while final stationary configurations may be reached at optical depths of thousands (Ioka et al. 2018). This is not really satisfied in the particular case: from $r\sigma_T n \sim c/V_s$, with V_s given by (17) and density by (4), the condition $\tau \sim c/V_s$ is satisfied for

$$t \leq \frac{L_{w,0}^{1/3} M_{ej}^{1/3} \sigma_T^{2/3}}{m_p^{2/3} c V_0} = 0.1 m_{ej,-2}^{1/3} \text{ days} \quad (25)$$

Thus, only at very early times the shock is highly radiation-dominated.

At the moment of shock breakout, at $t \leq 1$ day, we expect an X-ray flash with duration $\sim 10^4$ seconds, Eq. (25) and luminosities $\sim 10^{42} - 10^{43} \text{ erg s}^{-1}$ (e.g., Svirski & Nakar 2014). Later on, after the shock is no longer radiation

dominated, the post-shock temperature evaluates to

$$T_s = \frac{3}{16} m_p V_s^2 \approx \frac{m_p L_{w,0}^{1/2} V_0^{3/2} \sqrt{t}}{\sqrt{c M_{ej}}} = 5 \times 10^5 t_d^{1/2} m_{ej,-2}^{-1/2} \text{eV}. \quad (26)$$

The corresponding free-free luminosity is far too small $\sim 10^{35} m_{ej,-2}^{7/4} t_d^{-11/4} \text{ erg s}^{-1}$.

4.5. Anisotropy

Thus, optical emission is puzzling - it is hard to see how requirement of radiation-modified shocks (and hence large optical depth) can be reconciled with short transient time scales (and hence small optical depth). A possible answer is anisotropy. All the ingredients - pre-collapse wind, ejecta and the NS wind are expected to be anisotropic, see Fig. 1. First, the wind is launched by star that rotates with nearly critical velocity. Even Solar wind is highly anisotropic: slow and dense in the equatorial sector and fast in the polar regions (with approximately constant $d\dot{M}/d\Omega$). Second, the newly formed NS can, under certain parameters, be nearly critically spinning, so that the ejecta is anisotropic as well (see Lyutikov & Toonen 2017). Third, the remaining NS's wind is equatorially collimated, with power $\propto \sin^2 \theta$ (Michel 1973).

There are strong observational arguments in favor of anisotropy. First, hydrogen and helium lines show spectral asymmetry, with a tail towards longer wavelengths (Margutti et al. 2018). This can be explained if the line of sight samples unevenly the ejecta.

Anisotropic ejecta can also reconcile the requirements of low ejecta mass, $\sim 10^{-2} M_\odot$ (and hence early transparency) and the requirement of larger ejecta mass, to keep the NS wind-generated forward shock to be radiatively dominated, which would nicely explain the optical temperature, Eq. (24).

An alternative possibility is that the later optical emission originates as a synchrotron emission from particles accelerated at the forward shock. One can construct a model of particle acceleration at the forward shock following the standard GRB parametrization (*e.g.*, Piran 2004), with $\epsilon_B \sim 10^{-4}$, $\gamma \sim 10^3$, in the fast cooling regime (fast cooling for the forward shock is important - X-ray luminosity for the termination shock and optical from the forward shock are comparable, (Margutti et al. 2018). But the expected spectrum will be non-thermal.

5. The X-ray transient: synchrotron emission from the NS-driven termination shock

5.1. Typical frequencies

We associate the X-ray emission with the particles accelerated at the termination shock. Let us consider its properties next. Suppose the neutron star-launched wind is propagating with Lorentz factor γ_w . The peak synchrotron frequency of particles accelerated by the wind termination shock is then, using the estimate of the magnetic field (18),

$$\epsilon_s \approx \gamma_w^2 \hbar \frac{eB}{m_e c} = \sqrt{2} \frac{e\hbar}{m_e c^{5/4}} \gamma_w^2 \frac{L_{w,0} M_{ej}^{1/4}}{V_{ej,0}^{3/4}} \left(t^{5/4} \sqrt{1 + t/t_\Omega} \right)^{-1} = 50 \text{keV } m_{ej,-2}^{1/4} \gamma_{w,5}^2 \left(t_d^{5/4} \sqrt{1 + 0.05 t_d} \right)^{-1} \quad (27)$$

where t_d is time since explosion in days. It is sharply decreases with time. Thus, after \sim two weeks the injection peak passes through keV energy band. This is the hard X-ray component seen before \sim 2 weeks, (Fig. 6 in Margutti et al. 2018)

At ~ 40 days $\epsilon_{s,40d} \approx 300\gamma_{w,5}$. If at this moment the wind Lorentz factor falls to $\gamma_w \sim 5 \times 10^3$, then the injection falls in the near-IR. This explains the rising near-IR light curve after ≥ 40 days (Fig. 5 in [Perley et al. 2018](#)).

The cooling energy

$$\epsilon_c \approx \frac{\hbar m_e^5 c^9}{e^7 B^2 t^2} \quad (28)$$

is well below ϵ_s - the emission is in the fast cooling regime ([Sari et al. 1996](#)). Thus, a large fraction of the energy given to the accelerated particles is radiated. The high radiation efficiency of the termination shock in the post-explosion wind was previously stressed by [Lyutikov & Camilo Jaramillo \(2017\)](#).

5.2. Evolution of particle distribution in expanding post termination shock flow

The magnetic field in the post termination shock flow, Eq. (18), decreases with time. As a result, particles will first cool quickly, but later on the radiative losses will decrease. This will lead to effective pile of cooled previously injected particles at some low Lorentz factor. We suggest this as an origin of late radio peak. Let us first consider the case of constant wind luminosity, $t \leq t_\Omega$. Neglecting the adiabatic losses (radiative losses are much more important), the evolution of the particles' Lorentz factor is given by

$$\partial_t \gamma \approx -\frac{e^4}{m_e^3 c^5} B^2 \gamma^2 \quad (29)$$

with magnetic field give by (18). Solution of (29) for a particle injected at time t_{inj} with Lorentz factor γ_{inj} , at times $t \ll t_\Omega$ is then

$$\begin{aligned} \frac{\gamma}{\gamma_{inj}} &= (1 + \Delta \gamma_{inj})^{-1} \\ \Delta &= \frac{2}{3} \left(\left(\frac{t_0}{t_{inj}} \right)^{3/2} - \left(\frac{t_0}{t} \right)^{3/2} \right) \\ t_0 &= \left(\frac{3}{4} \frac{e^8}{m_e^6 c^{11}} \frac{L_{w,0} M_{ej}}{V_{ej,0}^3} \right)^{1/3} = 4 m_{ej,-2}^{1/3} \text{days} \end{aligned} \quad (30)$$

At times $t \gg t_\Omega$, when the magnetic field evolves differently with time, Eq (18)

$$\begin{aligned} \Delta &= \frac{2}{5} \left(\left(\frac{t_0}{t_{inj}} \right)^{5/2} - \left(\frac{t_0}{t} \right)^{5/2} \right) \\ t_0 &= \left(\frac{4e^8 t_\Omega^2 L_{w,0} M_{ej}}{c^{11} m_e^6 V_{ej,0}^3} \right)^{1/5} \end{aligned} \quad (31)$$

For particles injected at time t_{inj} with distribution function $f_{inj} \propto \gamma_{inj}^{-p}$ at $\gamma_{inj} > \gamma_{inj,min}$, at later times $t > t_{inj}$ the distribution function is given by

$$\begin{aligned} f &\propto \gamma^{-p} (1 - \Delta \gamma)^{p-2} \Theta(\gamma - \gamma_{min}) \Theta(\gamma_{max} - \gamma) \\ \gamma_{max} &= \frac{1}{\Delta} \\ \gamma_{min} &= \frac{\gamma_{inj,min}}{1 + \Delta \gamma_{inj,min}} \end{aligned} \quad (32)$$

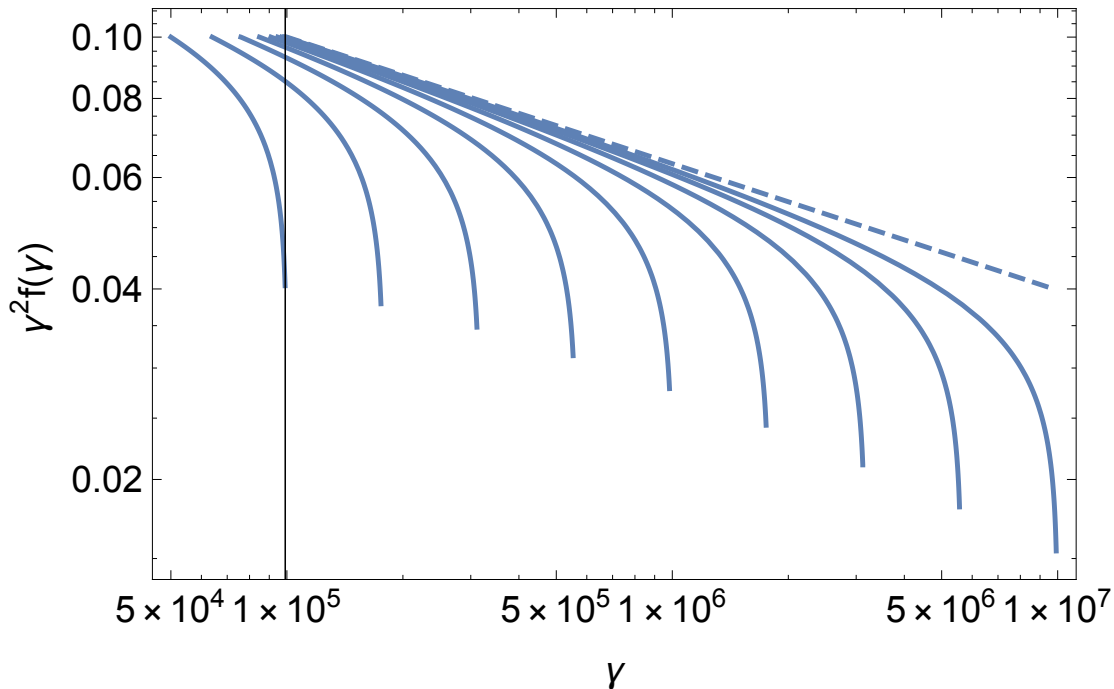


Fig. 2.— Evolution of the distribution function within a given injected shell in decreasing magnetic field. Dashed line is the injected spectrum, $p = 2.2$, $\gamma_{inj,min} = 10^5$. Curves are separated by equal steps in the parameter Δ , see Eq. (32) (not equal steps in time).

see Fig. (2)

At any moment the emission is contributed to by a distribution of particles with different injection energies, different injection times and different cooling history in the changing magnetic field. The outcome is bound to be complicated - the total distribution at any time t is given by integration of (32) over t_{inj} and injection rate. Qualitatively, particles that are injected early on cool quickly and do not contribute much to the later emission. On the other hand, particles that are injected late, find themselves in low magnetic field and also do not emit efficiently.

As a simple order-of-magnitude estimate, we can assume that all particles injected at some t_{inj} cool quickly to the minimal energy γ_{min} , Eq (32). For $t \gg t_{inj}$ the terminal Lorentz factors are

$$\gamma_{\infty} = \begin{cases} \frac{3}{2} \left(\frac{t_{inj}}{t_0} \right)^{3/2} & t < t_{\Omega} \\ \frac{5}{2} \left(\frac{t_{inj}}{t_0} \right)^{5/2} & t > t_{\Omega} \end{cases} \quad (33)$$

Then for constant injection rate we expected the distribution near the lowest energy range to be

$$f \propto \begin{cases} \gamma^{-1/3} & t < t_{\Omega} \\ \gamma^{-3/5} & t > t_{\Omega} \end{cases} \quad (34)$$

This will produce fluxes $F_{\nu} \propto \nu^{-(p-1)/2} \propto \nu^{1/3}$ and $\nu^{1/5}$ correspondingly. This exercise is not meant to produce a fit to data, but to demonstrate that cooling in decreasing magnetic field can produce rising spectral flux at the lower end of the spectrum.

6. Low frequency emission - free-free absorption in the ejecta and the wind

At lower frequencies, radio and IR waves can experience free-free absorption (Lang 1999, Eq. 1.223) both within the ejecta and in the pre-explosion wind.

Ejecta contribute to free-free absorption a lot

$$\tau_{ff,ej} = 2 \times 10^{20} m_{ej,-2}^4 \nu_{GHz}^{-4.2} T_4^{-2.7} t_d^{-10} \quad (35)$$

It is optically thin for very high frequencies for a long time

$$\nu_{GHz} > 7 \times 10^4 m_{ej,0.95} T_4^{-0.64} t_d^{-2.4} \quad (36)$$

Thus, in the radio and far IR the ejecta remains mostly opaque until the shock breakout from the ejecta, after approximately a month, Eq. (12).

The free-free optical depth through the wind, with density given by (1), becomes unity at

$$r_{ff,wind} = 1.5 \times 10^{16} \dot{m}_{-5}^{2/3} \nu_{GHz}^{-7/10} T_4^{-9/20} v_{w,8}^{-2/3} \quad (37)$$

The shock (16) reaches the optical depth of the order of unity through the pre-explosion wind, Eq (37), for

$$t = 8 \dot{m}_{-5}^{8/15} \nu_{GHz}^{-14/25} T_4^{-9/25} v_{w,8}^{-8/15} m_{ej,-2}^{1/5} \text{days} \quad (38)$$

The effects of free-free absorption explain the evolution of the radio and IR luminosities, see (Ho et al. 2018, Fig. 1). High frequencies, 341 and 230 GHz, are transparent all along, while lower frequency, 34 GHz traces the expanding radius of the corresponding $\tau = 1$ surface.

7. Population synthesis

7.1. Pre-merger evolutionary channels

Most calculations of WD-WD mergers are aimed at explaining the Type Ia SNe, thus *looking* for detonation (see Maoz et al. 2014, for a recent review). Less attention has been given to models that fail to detonate. As we argue, failed SN Ia, that collapse via electron capture, may be related to the FBOTs. Dan et al. (2014) discussed the results of the WD-WD mergers and argued that there is large phase space available for WD-WD mergers to produce an accretion induced collapse (AIC). Nomoto & Iben (1985) stressed the role of carbon ignition during WD mergers in order to produce a Type Ia SN. Thus, in order to avoid explosion, there should be little carbon in the system. We suggest then that the primary is a heavy ONeMg WD. In this section we calculate possible evolutionary scenarios and rates for the corresponding mergers.

We use the binary population synthesis (BPS) method to predict the properties of the binary mergers, that is the merger rates, host galaxies and formation channels. Using the BPS code `SeBa` (Portegies Zwart & Verbunt 1996; Toonen et al. 2012; Toonen & Nelemans 2013), we simulate the evolution of a large number of binaries following in detail those that lead to the merger of an ONeMg and CO WD. Processes such as wind mass loss, stable & unstable mass transfer, accretion, angular momentum loss, and gravitational wave emission are taken into account. It was shown by Toonen et al. (2014) that the main source of uncertainty in the BPS outcomes come from the uncertainty in the input assumptions, in particular the CE-phase. For this reason, we follow Toonen et al. (2012), in performing two sets of

population synthesis calculations using their model $\alpha\alpha$ and $\gamma\alpha$. For full details on the models, see [Toonen et al. \(2012\)](#). In short, these models differ from one another with respect to the modeling of the CE-phase. Despite the importance of this phase for the formation of compact binaries and the enormous effort of the community, the CE-phase is still poorly constrained (see [Ivanova et al. 2013](#), for a review). Commonly the CE-phase is modeled in BPS codes by energy conservation ([Webbink 1984](#)), with a parameter α that describes the efficiency with which orbital energy is consumed to unbind the CE. This recipe is used in model $\alpha\alpha$ for every CE-phase. An alternative model has been proposed by ([Nelemans et al. 2000](#)) in order to reproduce the observed population of double white dwarfs. This model is based on a balance of angular momentum with an efficiency parameter γ . In our model $\gamma\alpha$, the γ -recipe is used unless the binary contains a compact object or the CE is triggered by a tidal instability (rather than dynamically unstable Roche lobe overflow, as proposed by [Nelemans et al. \(2000\)](#) for detached double white dwarfs).

Figures 3-4 show the initial parameters of binaries leading to mergers between ONeMg and CO WDs in our simulations. Every point represents a single system in the BPS simulations. The figures show that there are different evolutionary paths that can lead to an ONe-CO WD merger, however the dominant channels involve initially compact systems (in blue circles) i.e. the 'inverted channel' and initially wide systems (in green squares) i.e the 'direct' channel. For single stars, the initial mass of the progenitor of an ONeMg WD ranges between approximately $6.5-8M_{\odot}$ according to [SeBa](#). This is similar to the range of initial masses in the direct channel where the primary forms the ONeMg WD (majority of green points in Fig. 3). The progenitors of ONeMg WDs in the 'inverted' channel, *i.e.*, the secondaries denoted in blue, have lower masses as these stars accrete a significant amount of mass from their companion stars.

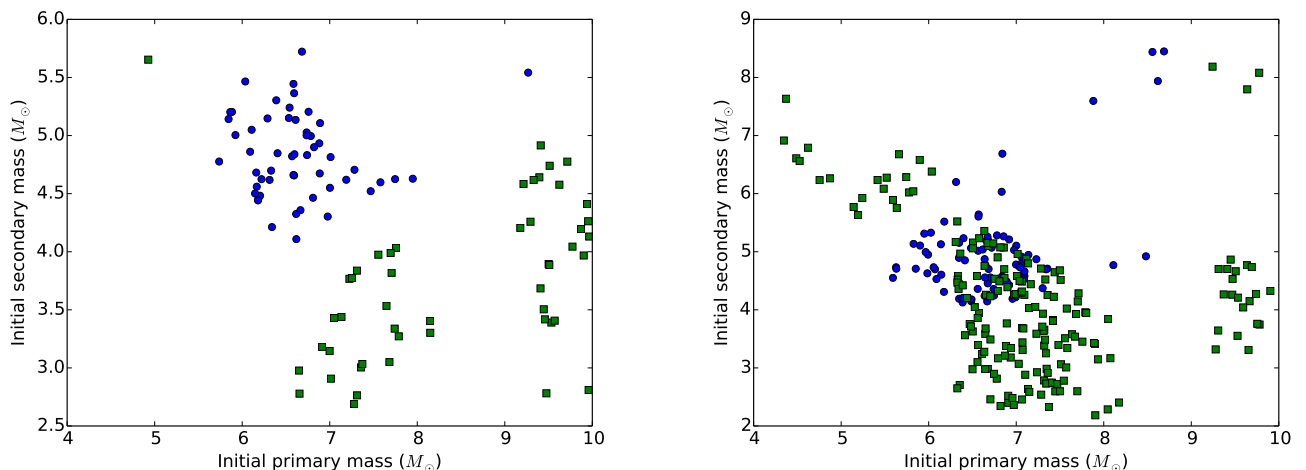


Fig. 3.— Distribution of initial masses for model $\gamma\alpha$ (left panel) and model $\alpha\alpha$ (right panel). The primary represents the first formed WD, secondary the last formed WD. With green squares the systems where the ONeMg WD is formed first, with blue circles where this is the last formed WD. In all models the systems marked in blue come from tight orbits where the first phase of mass transfer typically proceeds in a stable manner. The systems marked in green mostly originate from wider orbits, such that that first phase of mass transfer is likely a common-envelope phase.

In Fig. 5 we show the final masses of the ONeMg and CO WD that merge according to model $\alpha\alpha$ and $\gamma\alpha$ respectively. The masses of the ONeMg WDs are in the range $1.1 - 1.4M_{\odot}$, while the majority of CO WDs have masses in the range $0.5-0.8M_{\odot}$. As described above it is possible that the ONeMg WD forms before the other WD in the system (channel 'direct'), or it forms afterwards (channel 'inverted'). In model $\gamma\alpha$, 48% of merging ONe-CO DWDs go through the 'direct' channel, whereas for model $\alpha\alpha$ the fraction goes up to 69%. The masses of the CO WDs in the 'inverted'

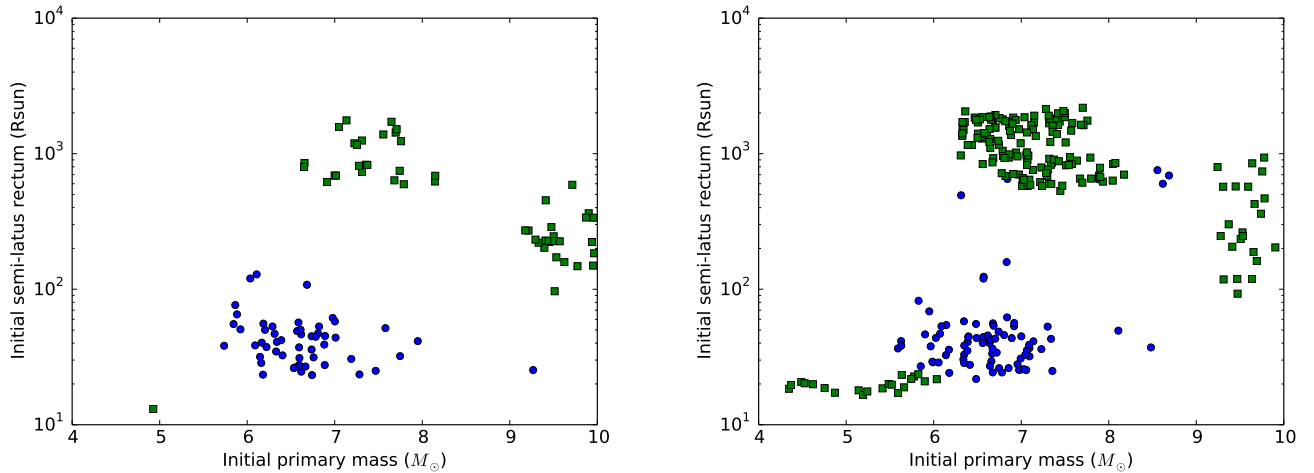


Fig. 4.— Distribution of initial semi-latus rectum for model $\gamma\alpha$ (left panel) and model $\alpha\alpha$ (right panel). The color coding is the same as in Fig. 3. In the case of $\alpha\alpha$, green dots at low orbital separations correspond to the systems in which the primary starts with $\sim 6M_{\odot}$ and relatively small separation, so that the first phase of mass transfer is stable. As the secondary accretes, it becomes more massive, its evolution speeds up, and it becomes a ONeMg WD while the primary is still a stripped (hydrogen poor helium-rich) nuclear burning star, which eventually becomes a WD. This is similar to the third evolution channel in [Toonen et al. \(2012\)](#).

channel are systematically higher than those of the 'direct' channel.

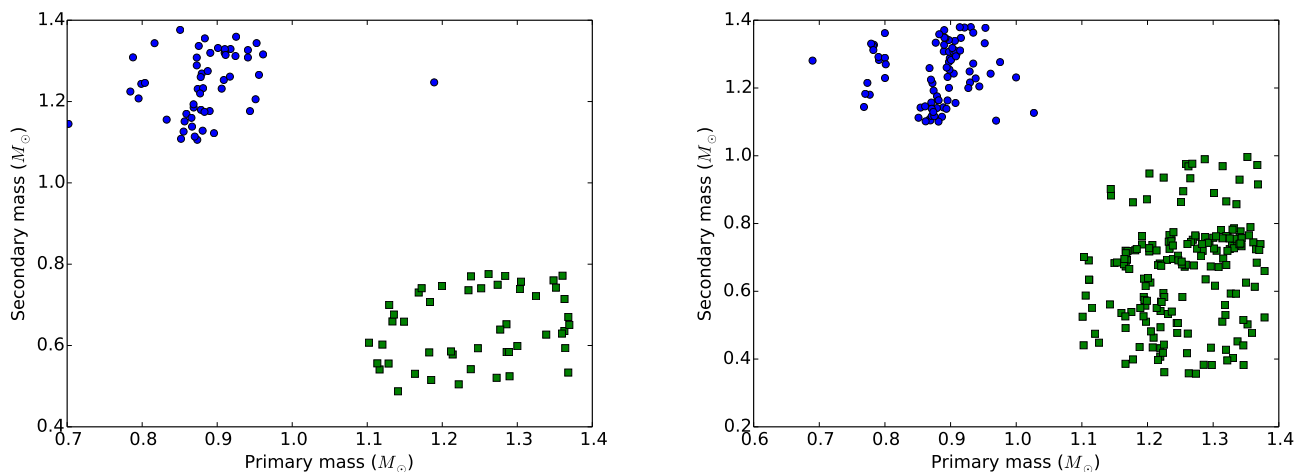


Fig. 5.— Distribution of masses for model $\gamma\alpha$ (left panel) and model $\alpha\alpha$ (right panel). The color coding is the same as in Fig. 3.

In Fig. 6 we show the distribution of the mass ratio as a function of the primary mass. For donor masses in the range $1.1 - 1.3M_{\odot}$ [Marsh et al. \(2004\)](#) (see their Fig. 1) find that mass transfer is always unstable if the companion mass is above ~ 0.6 . It is always stable for $\leq 0.2 - 0.4$. The blue systems are well above the limit for unstable mass transfer.

The green systems occupy a larger part of parameter space. The far majority of the systems have a mass ratio that make stable mass transfer unlikely. Also note that given the ‘optimistic’ stability limits of Marsh et al. (2004) the AM CVn rate is overestimated by orders of magnitude, indicating that mass transfer is likely less stable than the ‘optimistic scenario’. In addition, the results from Marsh et al. (2004) do not take into account the effect of novae outbursts on the evolution of the systems. As shown by Shen et al. (2012) these outburst have a destabilizing effect on the mass transfer.

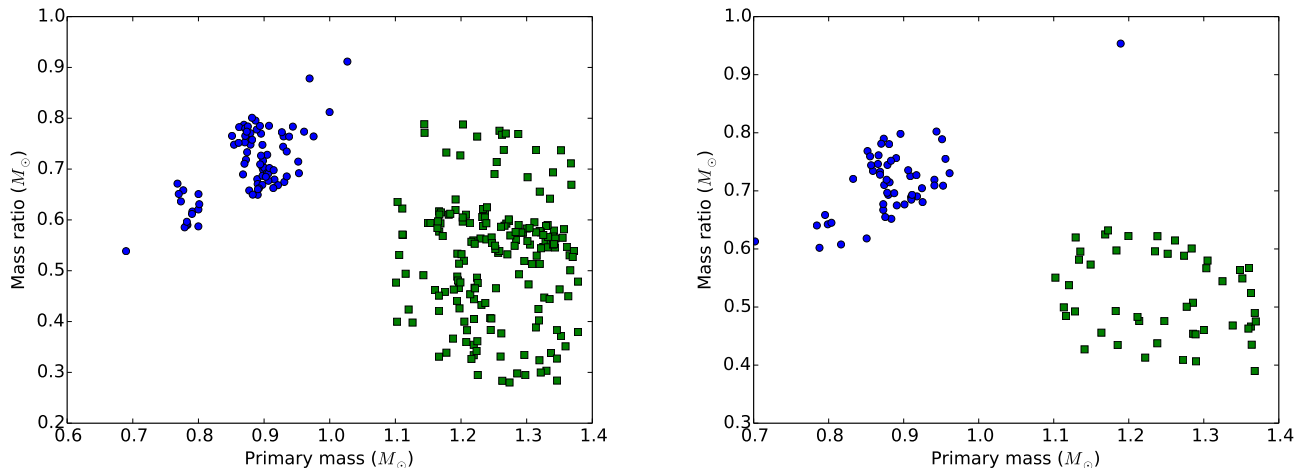


Fig. 6.— Distribution of the mass ratio as a function of the primary mass for model $\gamma\alpha$ (left panel) and model $\alpha\alpha$ (right panel). The color coding is the same as in Fig. 3.

7.2. Rates

Using the BPS simulations, we also estimate the rate of CO-ONeMg WD mergers. Assuming a constant star formation history of $4M_{\odot} \text{ yr}^{-1}$ for a Hubble time (roughly alike the Milky Way), the current merger rate ranges from $1.4 \times 10^{-4} \text{ yr}^{-1}$ for model $\alpha\gamma$ and $3.4 \times 10^{-4} \text{ yr}^{-1}$ for model $\alpha\alpha$. This is in agreement with the BPS calculations of Yungelson & Kuranov (2017) and Ruiter et al. (2018). The CO-ONeMg are less common than mergers between CO-CO WDs for which we find a merger rate of $4.5 \times 10^{-3} \text{ yr}^{-1}$. Mergers of CO-CO WDs with a combined mass above Chandrasekhar - the classical supernova type Ia progenitors (Webbink 1984; Iben & Tutukov 1984) have a merger rate of $1.7 - 2.2 \times 10^{-3} \text{ yr}^{-1}$ in our simulations, about an order of magnitude above that of CO-ONeMg WDs.

Integrated over time, the total number of CO-ONeMg WD mergers ranging between $(3.5 - 8.6) \cdot 10^{-5}$ per Solar mass of created stars². The rate of FBOTs has been estimated by Drout et al. (2014) to be 4%-7% of core-collapse supernova. Assuming the core-collapse rate is about $0.0025\text{-}0.010 M_{\odot}^{-1}$ (Maoz & Graur 2017; Horiuchi et al. 2011; Graur et al. 2017)³, the estimated CO-ONeMg WD merger rate is consistent with the lower limit of the FBOT rate.

²This is independent of the assumed star formation history.

³The upper limit is calculated by Maoz & Graur (2017). The lower limit is based on the observed supernova type Ia rate $((1.3 \pm 0.1) \cdot 10^{-3} M_{\odot}^{-1})$ (Maoz & Graur 2017) and the ratio of core-collapse to type Ia supernova (0.25-4 Graur et al. 2017)

7.3. Host galaxies

In Fig. 7 we show the distributions of delay times of the CO-ONeMg mergers after a single burst of starformation. Their merger rates peaks at short delay times of about $\sim 50\text{-}100\text{Myr}$, with a long tail to long delay times. The peak occurs significantly earlier than expected from the classical type Ia supernovae progenitors consisting of superChandrasekhar mergers of CO-CO WDs (consistent with Yungelson & Kuranov 2017; Ruiter et al. 2018). The typical delay time of the CO-ONeMg mergers is closer to that of core-collapse supernovae, which peaks sharply at $\sim 50\text{Myr}$ (see e.g. Fig.3 of Zapartas et al. 2017). As a result, we expect the host galaxies of CO-ONeMg mergers to be more similar to those of core-collapse supernovae instead of Type Ia supernovae. This is consistent with the observed host galaxies of FBOTs (Drout et al. 2014).

8. Alternatives

An alternative to the WD merger scenario is the possibility of ultra-stripped envelopes in close binaries (Tauris et al. 2013, 2015). Binary interactions may strip the primary star of the envelope and also affect the mass of the collapsing core (Langer 2012; Podsiadlowski et al. 2004). Müller et al. (2018a,b) estimate that ultra-stripped SNe produce normal slowly rotating pulsars, which are unlikely to produce fast spinning central neutron star. Müller et al. (2018a) studied the case when the angular momentum is implanted onto the neutron star only due to accretion of a tenuous envelope, without accounting for the progenitor’s initial spins. In contrast, in the case of double WD merger the envelope has a lot of angular momentum and has time to implant it to the core during the shell burning stage.

In a possibly related line of research, Piran & Shaviv (2005), see also Dall’Osso et al. (2014), argued that the pulsar J0737-3039B was born through non-standard SN mechanism (presumably via AIC), similar to the ultra-stripped case considered by Tauris et al. (2015). Piran & Shaviv (2005) also argued for slow initial spin (and slow kick velocity). Thus, ultra-stripped binary cores produce slowly rotating remnants, while AT2018cow needs a powerful central source.

9. Discussion

In this paper we discuss a channel for transient emission after electron-capture collapse following a merger of two WDs. Qualitatively, this channels allows a collapse into a neutron star to occur with a small envelope mass. As a result the ejecta is light, have high velocity and becomes optically transparent much earlier. This early transparency allows higher radiation efficiency, as energy is not spent on adiabatic expansion of the envelope. In addition, light envelopes allow more efficient conversion of the rotational energy of the central engine - presumably a neutron star - into radiation. (If the envelope remains optically thick for along time any wind energy is spent on matter acceleration, not production of radiation. Also, large envelope can slow down the central neutron star in a propeller regime.)

Thus, small envelope mass, and small ejecta mass, lead to brighter and shorter SNe. In AT2018cow the ejecta was the lightest, with only $\sim 10^{-2}M_{\odot}$ ejected. In this case the AIC occurred at the time when most of the envelope was already lost to the wind. Other FBOTs may have larger remaining envelopes at the moment of AIC and larger ejected masses, but all smaller than $\sim 0.5M_{\odot}$. In our model the envelop mass depends on the mass of the primary ONeMg WD (how close it is to the Chandrasekhar limit), and the mass of the companion (how quickly mass is added to the core, mass loss rate - how long the shell burning continues).

We also advocate the Pulsar Wind paradigm - the reverse shock, as opposed to the forward shock - as the origin of the X-ray emission, similar to the GRB model of Lyutikov & Camilo Jaramillo (2017); see also Usov (1992); Lyutikov (2006b); Metzger et al. (2011).

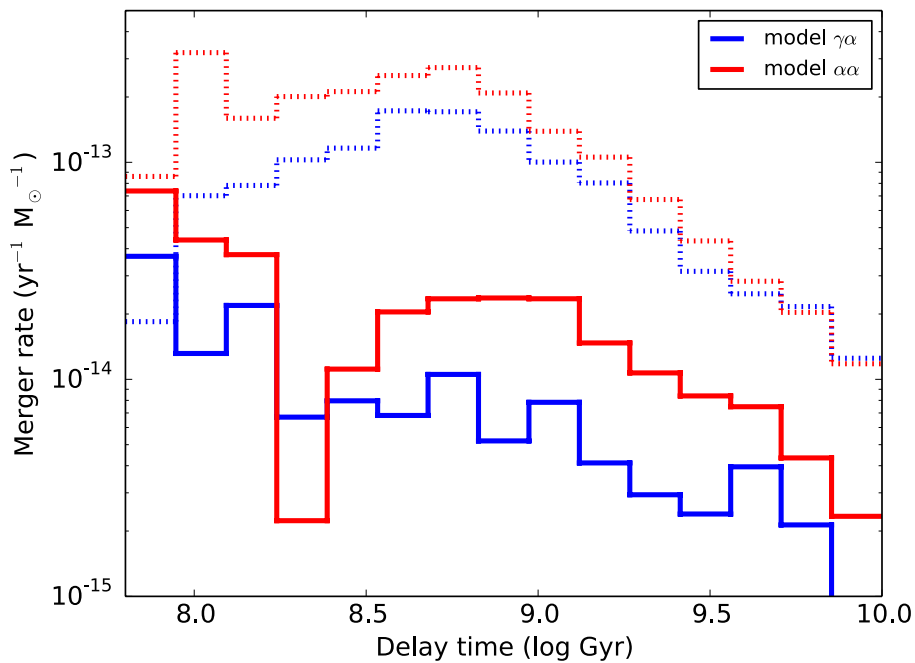


Fig. 7.— Delay time distribution of the CO-ONeMg WD mergers (solid lines) for two models of common-envelope evolution. Model $\gamma\alpha$ is shown in blue, and model $\alpha\alpha$ in red. For comparison the super-Chandrasekhar mergers of CO-CO WDs is shown with dotted lines. These typically occur at later delay times than the CO-ONeMg WD mergers.

Let us highlight how the key observational results discussed by [Margutti et al. \(2018\)](#) are explained in our model

- A very short rise time to peak, $t_{\text{rise}} \sim \text{few days}$ - optical transient is generated by an envelope ejected during the bounce from the proto-neutron star. Ejected mass is small, while velocity is nearly relativistic (of the order of the escape velocity from the surface of a proto-neutron star).
- Large bolometric peak luminosity - as the ejecta becomes optically thin early on, a large fraction of the internal energy is emitted (as opposed to been spent on adiabatic expansion in conventional SN explosion).
- Persistent blue colors, with lack of evidence for cooling at $\delta t \gtrsim 30$ days - later-on the emission starts to become dominated by the non-thermal particles accelerators at the termination shock.
- Large blackbody radius $R_{\text{bb}} \sim 8 \times 10^{14}$ cm - wind-driven cavity expands to these scales on time scales of few days, Eq. (16).
- Persistent optically thick UV/optical emission with no evidence for transition into a nebular phase - emission is dominated by the radiation-modified forward shock.
- Abrupt change of the velocity of the material which dominates the emission at times ≥ 20 days - the jet breaks through the ejecta and enters the pre-explosion wind, after time given by (12).
- NIR excess of emission - injection energy at the termination shock moved to IR both due to decreasing magnetic field in the post-shock flow and falling Lorentz factor of the wind, Eq. (27) and discussion afterwards.
- The spectra evolve from a hot, blue, and featureless continuum around the optical peak, to very broad features - this is a transition from radiation-modified forward shock at early time to regular matter-dominated forward shock, combined with emission from the termination shock.

In addition

- “Late-time optical spectra at $t > 20$ days show line widths of 4000 km s^{-1} ($0.01c$, indicating substantially lower outflow velocities than at earlier times (when $v = 0.1c$), and an abrupt transition from very high velocity to lower velocity emitting material” (Margutti et al. 2018). We associate this transition with the moment that the NS-driven shock plows through the ejecta and enters the pre-collapse wind, Eq. (12) - this is due to slowing down of the ejecta.
- There are indication of hydrogen later-on (Margutti et al. 2018) - if the disrupted WD was of the DA type - one expects some hydrogen in the pre-collapse wind, of the order of $10^{-4} M_{\odot}$ total. This explains the late appearance of hydrogen lines, presumably when the NS-driven forward shock exits the ejecta and enters the pre-existing wind. (We have no way of telling what the atmosphere of a post interaction WD will be. However, it is probable that the majority will be a DA, and therefore the rates would not be wildly different from the ones presented here.)
- Similar X-ray and optical luminosities are naturally explained as emission from forward and NS wind termination shocks (the latter in the fast cooling regime).
- Early X-ray spectral bump is also due to the passage of the peak frequency (late similar effect will produce IR increase)
- Erratic inter-day variability of the X-ray emission (Ho et al. 2018) is hard to reproduce within the forward shock scenario (Lyutikov 2006b), since the forward shock emission properties depend on the *integrated* quantities - central engine total energy and total matter swept. But they can be reproduced within the internal shock paradigm - in the fast cooling regime - either by the changes of the wind properties of the central source (Lyutikov & Camilo Jaramillo 2017), minijets in the outflow (Lyutikov 2006a), or by Crab flare-like reconnection processes in the shocked pulsar wind (Clausen-Brown & Lyutikov 2012; Lyutikov et al. 2018).

- We associate both the high energy as well radio emission not with the forward shock, as is the case of in regular SNe (Weiler et al. 1986; Chevalier 1998), but with reverse shock in the newly formed PWN. As a result, the temporal evolution will be different.

Also note, that AIC with a formation of a neutron star is probably responsible for formation of young pulsars in globular clusters Lyne et al. (1996). This is consistent with the present model.

The present model, connecting FBOTs to the merger of WDs, is related to the possibility that *some* short GRBs come from a similar channel of WD mergers (Lyutikov & Toonen 2017). The detection of gravitational waves associated with a GRB (Abbott et al. 2017) identifies merger of neutron stars as the central engine. It is not clear at the moment whether this identification is generic to the whole class of short GRBs. As discussed by Lyutikov (2009); Lyutikov & Toonen (2017), there is a number of observational contradictions to the binary neutron star merger paradigm (like extended emission and late flares - both not seen in GW/GRB170817). One possibility, that is still viable, is that some short GRBs originate from WD mergers. Several parameters may separate outcomes of WD mergers (*e.g.*, FBOTs and short GRBs): masses of the merging WDs, the amount of the material lost to the wind, spin right before the AIC (so that AIC can either occur directly to a neutron star or with a formation of an accretion disk). For preferential intrinsic parameters and viewing angles (*e.g.*, observer along the spin axis of the collapsing WD) we may see a short GRB and later on an FBOT.

Acknowledgments

This work had been supported by DoE grant DE-SC0016369 and NASA grant 80NSSC17K0757.

We would like to thank Maxim Barkov, Ori Fox, Raffaella Margutti, Danny Milisavljevic, Amir Levinson, Eran Ofek, Amir Sharon, Nir Shaviv and Thomas Tauris for discussions.

REFERENCES

- Abbott, B. P., Abbott, R., Abbott, T. D., Acernese, F., Ackley, K., Adams, C., Adams, T., Addesso, P., Adhikari, R. X., Adya, V. B., & et al. 2017, Physical Review Letters, 119, 161101
- Abdikamalov, E. B., Ott, C. D., Rezzolla, L., Dessart, L., Dimmelmeier, H., Marek, A., & Janka, H.-T. 2010, Phys. Rev. D, 81, 044012
- Arnett, W. D. 1982, ApJ, 253, 785
- Balsara, D. S., Fisker, J. L., Godon, P., & Sion, E. M. 2009, ApJ, 702, 1536
- Belyaev, M. A., Rafikov, R. R., & Stone, J. M. 2013, ApJ, 770, 67
- Brooks, J., Schwab, J., Bildsten, L., Quataert, E., Paxton, B., Blinnikov, S., & Sorokina, E. 2017, ApJ, 850, 127
- Budnik, R., Katz, B., Sagiv, A., & Waxman, E. 2010, ApJ, 725, 63
- Canal, R., & Schatzman, E. 1976, A&A, 46, 229
- Chevalier, R. A. 1998, ApJ, 499, 810
- Clausen-Brown, E., & Lyutikov, M. 2012, MNRAS, 426, 1374

- Dall’Osso, S., Piran, T., & Shaviv, N. 2014, *MNRAS*, 438, 1005
- Dan, M., Rosswog, S., Brüggén, M., & Podsiadlowski, P. 2014, *MNRAS*, 438, 14
- Drout, M. R., Chornock, R., Soderberg, A. M., Sanders, N. E., McKinnon, R., Rest, A., Foley, R. J., Milisavljevic, D., Margutti, R., Berger, E., Calkins, M., Fong, W., Gezari, S., Huber, M. E., Kankare, E., Kirshner, R. P., Leibler, C., Lunnan, R., Mattila, S., Marion, G. H., Narayan, G., Riess, A. G., Roth, K. C., Scolnic, D., Smartt, S. J., Tonry, J. L., Burgett, W. S., Chambers, K. C., Hodapp, K. W., Jedicke, R., Kaiser, N., Magnier, E. A., Metcalfe, N., Morgan, J. S., Price, P. A., & Waters, C. 2014, *ApJ*, 794, 23
- Fryer, C., Benz, W., Herant, M., & Colgate, S. A. 1999, *ApJ*, 516, 892
- Graur, O., Bianco, F. B., Huang, S., Modjaz, M., Shivvers, I., Filippenko, A. V., Li, W., & Eldridge, J. J. 2017, *ApJ*, 837, 120
- Ho, A. Y. Q., Phinney, E. S., Ravi, V., Kulkarni, S. R., Petitpas, G., Emonts, B., Bhalerao, V., Blundell, R., Cenko, S. B., Dobie, D., Howie, R., Kamraj, N., Kasliwal, M. M., Murphy, T., Perley, D. A., Sridharan, T. K., & Yoon, I. 2018, *ArXiv e-prints*
- Horiuchi, S., Beacom, J. F., Kochanek, C. S., Prieto, J. L., Stanek, K. Z., & Thompson, T. A. 2011, *ApJ*, 738, 154
- Iben, Jr., I., & Tutukov, A. V. 1984, *ApJS*, 54, 335
- Inogamov, N. A., & Sunyaev, R. A. 1999, *Astronomy Letters*, 25, 269
- . 2010, *Astronomy Letters*, 36, 848
- Ioka, K., Levinson, A., & Nakar, E. 2018, *arXiv e-prints*
- Ito, H., Levinson, A., Stern, B. E., & Nagataki, S. 2018, *MNRAS*, 474, 2828
- Ivanova, N., Justham, S., Chen, X., De Marco, O., Fryer, C. L., Gaburov, E., Ge, H., Glebbeek, E., Han, Z., Li, X.-D., Lu, G., Marsh, T., Podsiadlowski, P., Potter, A., Soker, N., Taam, R., Tauris, T. M., van den Heuvel, E. P. J., & Webbink, R. F. 2013, *A&A Rev.*, 21, 59
- Jones, S., Röpke, F. K., Pakmor, R., Seitenzahl, I. R., Ohlmann, S. T., & Edelmann, P. V. F. 2016, *A&A*, 593, A72
- Kitaura, F. S., Janka, H.-T., & Hillebrandt, W. 2006, *A&A*, 450, 345
- Kompaneets, A. S. 1960, *Soviet Physics Doklady*, 5, 46
- Landau, L. D., & Lifshitz, E. M. 1959, *Fluid mechanics*
- Lang, K. R. 1999, *Astrophysical formulae*
- Langer, N. 2012, *ARA&A*, 50, 107
- Lyne, A. G., Manchester, R. N., & D’Amico, N. 1996, *ApJ*, 460, L41
- Lyutikov, M. 2006a, *MNRAS*, 369, L5
- . 2006b, *New Journal of Physics*, 8, 119
- . 2009, *ArXiv e-prints*

—. 2018, *MNRAS*, 477, 816

Lyutikov, M., & Camilo Jaramillo, J. 2017, *ApJ*, 835, 206

Lyutikov, M., Komissarov, S., & Sironi, L. 2018, *Journal of Plasma Physics*, 84, 635840201

Lyutikov, M., & Toonen, S. 2017, *ArXiv e-prints*

Maoz, D., & Graur, O. 2017, *ApJ*, 848, 25

Maoz, D., Mannucci, F., & Nelemans, G. 2014, *ARA&A*, 52, 107

Margutti, R., Metzger, B. D., Chornock, R., Vurm, I., Roth, N., Grefenstette, B. W., Savchenko, V., Cartier, R., Steiner, J. F., Terreran, G., Migliori, G., Milisavljevic, D., Alexander, K. D., Bietenholz, M., Blanchard, P. K., Bozzo, E., Brethauer, D., Chilingarian, I. V., Coppejans, D. L., Ducci, L., Ferrigno, C., Fong, W., Götz, D., Guidorzi, C., Hajela, A., Hurley, K., Kuulkers, E., Laurent, P., Mereghetti, S., Nicholl, M., Patnaude, D., Ubertini, P., Banovetz, J., Bartel, N., Berger, E., Coughlin, E. R., Eftekhari, T., Frederiks, D. D., Kozlova, A. V., Laskar, T., Svinkin, D. S., Drout, M. R., Macfadyen, A., & Paterson, K. 2018, *ArXiv e-prints*

Marsh, T. R., Nelemans, G., & Steeghs, D. 2004, *MNRAS*, 350, 113

Metzger, B. D., Giannios, D., Thompson, T. A., Bucciantini, N., & Quataert, E. 2011, *MNRAS*, 413, 2031

Michel, F. C. 1973, *ApJ*, 180, L133

Miyaji, S., Nomoto, K., Yokoi, K., & Sugimoto, D. 1980, *PASJ*, 32, 303

Mösta, P., Ott, C. D., Radice, D., Roberts, L. F., Schnetter, E., & Haas, R. 2015, *Nature*, 528, 376

Müller, B., Gay, D. W., Heger, A., Tauris, T. M., & Sim, S. A. 2018a, *MNRAS*, 479, 3675

Müller, B., Tauris, T. M., Heger, A., Banerjee, P., Qian, Y.-Z., Powell, J., Chan, C., Gay, D. W., & Langer, N. 2018b, *ArXiv e-prints*

Nelemans, G., Verbunt, F., Yungelson, L. R., & Portegies Zwart, S. F. 2000, *A&A*, 360, 1011

Nomoto, K., & Iben, Jr., I. 1985, *ApJ*, 297, 531

Nomoto, K., & Kondo, Y. 1991, *ApJ*, 367, L19

Ofek, E. O., Rabinak, I., Neill, J. D., Arcavi, I., Cenko, S. B., Waxman, E., Kulkarni, S. R., Gal-Yam, A., Nugent, P. E., Bildsten, L., Bloom, J. S., Filippenko, A. V., Forster, K., Howell, D. A., Jacobsen, J., Kasliwal, M. M., Law, N., Martin, C., Poznanski, D., Quimby, R. M., Shen, K. J., Sullivan, M., Dekany, R., Rahmer, G., Hale, D., Smith, R., Zolkower, J., Velur, V., Walters, R., Henning, J., Bui, K., & McKenna, D. 2010, *ApJ*, 724, 1396

Perley, D. A., Mazzali, P. A., Yan, L., Cenko, S. B., Gezari, S., Taggart, K., Blagorodnova, N., Fremling, C., Mockler, B., Singh, A., Tominaga, N., Tanaka, M., Watson, A. M., Ahumada, T., Anupama, G. C., Ashall, C., Becerra, R. L., Bersier, D., Bhallerao, V., Bloom, J. S., Butler, N. R., Copperwheat, C., Coughlin, M. W., De, K., Drake, A. J., Duev, D. A., Frederick, S., Jesús González, J., Goobar, A., Heida, M., Ho, A. Y. Q., Horst, J., Hung, T., Itoh, R., Jencson, J. E., Kasliwal, M. M., Kawai, N., Kulkarni, S. R., Kumar, B., Kumar, H., Kutuyrev, A. S., Khanam, T., Lee, W. H., Maeda, K., Mahabal, A., Murata, K. L., Neill, J. D., Ngeow, C.-C., Penprase, B., Pian, E., Quimby, R., Ramirez-Ruiz, E., Richer, M., Román-Zúñiga, C. G., Srivastava, S., Socia, Q., Sollerman, J., Tachibana, Y., Taddia, F., Tinyanont, K., Troja, E., Ward, C., & Wee, J. 2018, *ArXiv e-prints*

- Philippov, A. A., Rafikov, R. R., & Stone, J. M. 2016, *ApJ*, 817, 62
- Piran, T. 2004, *Reviews of Modern Physics*, 76, 1143
- Piran, T., & Shaviv, N. J. 2005, *Physical Review Letters*, 94, 051102
- Podsiadlowski, P., Langer, N., Poelarends, A. J. T., Rappaport, S., Heger, A., & Pfahl, E. 2004, *ApJ*, 612, 1044
- Portegies Zwart, S. F., & Verbunt, F. 1996, *A&A*, 309, 179
- Ruiter, A. J., Ferrario, L., Belczynski, K., Seitenzahl, I. R., Crocker, R. M., & Karakas, A. I. 2018, arXiv e-prints
- Sari, R., Narayan, R., & Piran, T. 1996, *ApJ*, 473, 204
- Shen, K. J., Bildsten, L., Kasen, D., & Quataert, E. 2012, *ApJ*, 748, 35
- Smartt, S. J., Clark, P., Smith, K. W., McBrien, O., Maguire, K., O’Neil, D., Fulton, M., Magee, M., Prentice, S., Colin, C., Tonry, J., Denneau, L., Stalder, B., Heinze, A., Weiland, H., Flewelling, H., & Rest, A. 2018, *The Astronomer’s Telegram*, 11727
- Svirski, G., & Nakar, E. 2014, *ApJ*, 788, 113
- Tauris, T. M., Langer, N., Moriya, T. J., Podsiadlowski, P., Yoon, S.-C., & Blinnikov, S. I. 2013, *ApJ*, 778, L23
- Tauris, T. M., Langer, N., & Podsiadlowski, P. 2015, *MNRAS*, 451, 2123
- Timmes, F. X., & Woosley, S. E. 1992, *ApJ*, 396, 649
- Toonen, S., Claeys, J. S. W., Mennekens, N., & Ruiter, A. J. 2014, *A&A*, 562, A14
- Toonen, S., & Nelemans, G. 2013, *A&A*, 557, A87
- Toonen, S., Nelemans, G., & Portegies Zwart, S. 2012, *A&A*, 546, A70
- Usov, V. V. 1992, *Nature*, 357, 472
- Weaver, T. A. 1976, *ApJS*, 32, 233
- Webbink, R. F. 1984, *ApJ*, 277, 355
- Weiler, K. W., Sramek, R. A., Panagia, N., van der Hulst, J. M., & Salvati, M. 1986, *ApJ*, 301, 790
- Woosley, S. E., & Baron, E. 1992, *ApJ*, 391, 228
- Yungelson, L. R., & Kuranov, A. G. 2017, *MNRAS*, 464, 1607
- Zapartas, E., de Mink, S. E., Izzard, R. G., Yoon, S.-C., Badenes, C., Götberg, Y., de Koter, A., Neijssel, C. J., Renzo, M., Schootemeijer, A., & Shrotriya, T. S. 2017, *A&A*, 601, A29